Terahertz beam propagation measured through three-dimensional amplitude profile determination

Matthew T. Reiten, Stacee A. Harmon, and Richard Alan Cheville

School of Electrical and Computer Engineering, Oklahoma State University

Received November 14, 2002; revised manuscript received March 17, 2003

To determine the spatio-temporal field distribution of freely propagating terahertz bandwidth pulses, we measure the time-resolved electric field in two spatial dimensions with high resolution. The measured, phase-coherent electric-field distributions are compared with an analytic model in which the radiation from a dipole antenna near a dielectric interface is coupled to free space through a spherical lens. The field external to the lens is limited by reflection at the lens–air dielectric interface, which is minimized at Brewster's angle, leading to an annular field pattern. Field measurements compare favorably with theory. Propagation of terahertz beams is determined both by assuming a $\mathrm{TEM}_{0,0}$ Gaussian profile as well as expanding the beam into a superposition of Laguerre–Gauss modes. The Laguerre–Gauss model more accurately describes the beam profile for free-space propagation and after propagating through a simple optical system. The accuracy of both models for predicting far-field beam patterns depend upon accurately measuring complex field amplitudes of terahertz beams. © 2003 Optical Society of America

OCIS codes: 260.3090, 320.7160.

1. INTRODUCTION

Photolithographically fabricated micrometer-scale antenna structures gated with ultrashort optical pulses have demonstrated the ability to generate and measure subpicosecond pulses of electromagnetic radiation phase coherently.[1,2] The spectral bandwidth of these pulses extends from below 100 GHz to above 4 THz, enabling a wide variety of experimental measurements based on terahertz time-domain spectroscopy (THz-TDS). These measurements include determination of rotational line shapes,[3] noncontact characterization of semiconductors,[4] electromagnetic scattering,[5] and THz-frequency imaging.[6] THz pulses have demonstrated efficient propagation when coupled to waveguides enabling low-loss, dispersion-free propagation over distances of tens of centimeters.[7]

Since the precise measurement of the time-resolved electric field is critical to THz-TDS, it is important to understand how beam propagation affects the temporal profile of THz pulses. A number of authors have looked at the effect of free-space propagation on the temporal characteristics of THz pulses. Near-single-cycle pulses have been predicted to temporally reshape on propagation through free space.[8,9] Temporal reshaping in an optical system has been predicted[10,11] and experimentally measured.[12,13] Since THz-TDS measures pulses' phase coherently, the Gouy phase shift accumulated at a beam focus is observable.[14,15] Pulse reshaping has also been observed on propagation of a THz pulse through an aperture.[16]

The temporal pulse reshaping depends strongly on the spatial profile of the THz beam. Measurements of the spatial profile of THz beams has been performed along a line orthogonal to the propagation vector[17–21]; the THz radiation pattern was found to be adequately represented by a Gaussian with a waist determined by the aperture of the silicon lens used to collimate the THz radiation. This is an important result since, by approximating the THz beam as a Gaussian, the $ABCD$ formalism[22,23] can be applied to determine temporal beam reshaping.[10,12] The $ABCD$ formalism provides a simple and mathematically tractable approach to calculate the effect of any paraxial optical system on a THz beam.

In some cases, it is important to know the accuracy of this first-order approximation. For example, in THz-TDS, an inherent assumption is that the frequency response of the detector to the incident beam does not change on insertion of the sample. This is a valid assumption if the frequency-dependent spatial profile of the THz beam incident on the detector remains unchanged when the sample is placed in the beam. However, thick samples with high index do change the spatial beam profile. The effect of beam profiles is even more important in other THz measurements, such as measurements of electromagnetic scattering.[5] In electromagnetic scattering measurements, the spatial profile of the incident radiation is critical to ensure even target illumination and calculating the scattered field. The spatial profile is also critical for coupling THz pulses to waveguides since an overlap integral of the spatial field profile with the waveguide modes determines the coupling efficiency.[24]

Here we experimentally investigate the propagation of THz beams. We extend previous measurements in two dimensions (linear position, time) to three dimensions by measuring the time-resolved electric field in time on a plane orthogonal to the direction of propagation. These measurements are compared with calculated beam profiles both near the THz source and in the far field. Measurements of field distribution at several source–detector spacings are performed to develop a simple model to pre-

0740-3224/2003/102215-11$15.00 © 2003 Optical Society of America

dict the spatial beam profile as the beam propagates. By using both TEM_{00} and higher-order Gaussian modes to model spatio-temporal evolution of THz beams, we seek to determine how accurate the lowest-order TEM_{00} approximation is to describe THz beam propagation.

2. DIPOLE-SILICON LENS ANTENNA PATTERN MODEL

To understand the propagation of our THz beam, we first discuss a model to determine the electric-field pattern of a lens-coupled antenna for the case of broad-bandwidth THz radiation. The lens-coupled dipole antenna structure used for generation and detection of THz radiation is shown in Fig. 1(a). The electric field distribution of the THz pulse at a given point in free space is determined by diffraction of the electric-field distribution on the silicon lens,[17,18,21] in turn determined by the electric field pattern of a dipole radiator at a planar dielectric boundary.

The spatial power distribution of a dipole radiator near a plane dielectric interface has been calculated analytically by Lukosz.[25] The vectorial electric-field distributions have also been expressed analytically in integral form[26]; however, the integrals are difficult to determine accurately due to singularities.[27] Here we take the approach taken by several previous authors,[17,18,27] treating radiation from the dipole as a superposition of plane waves, and finding the field external to the lens using the Fresnel relations as illustrated in Fig. 1(a).

At the internal surface of the silicon coupling lens, the field, $E_{\mathrm{INT}}(\omega)$, is due to a superposition of direct radiation from the dipole, $E_{\mathrm{DIR}}(\omega)$, and that reflected from the planar substrate–air interface, $E_{\mathrm{RFL}}(\omega)$. Ignoring the small far-field contribution polarized along the radial direction, the field $E_{\mathrm{DIR}}(\omega)$ at the lens is $\hat{\theta}$ polarized.[28] At incidence angles θ beyond the critical angle ($\theta_c = 16°$ for the GaAs–air interface at THz frequencies), the field reflected from the planar interface undergoes a phase shift determined by complex Fresnel reflection coefficients, r_s and r_p,[29] and the relative magnitudes of the S- and P-polarized components of the $\hat{\theta}$ oriented field with respect to the interface. In the plane containing the $\hat{x}$-oriented dipole and the $\hat{z}$ axis, the far field is wholly P polarized, while in the plane orthogonal to the dipole $(\hat{y}\hat{z})$, the field is S polarized.[27] The phase shift for reflections at angles greater than critical angle corresponds to a change in polarization of $E_{\mathrm{RFL}}(\omega)$ from linear to elliptical polarization.

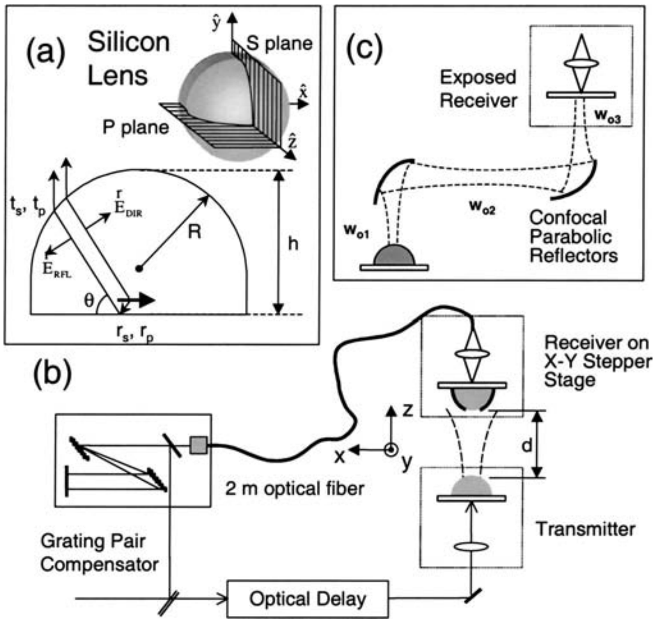

Fig. 1. (a) Detail of silicon-lens system used to model field pattern at waist. (b) The experimental setup for measuring the spatially and temporally resolved electric fields. (c) Imaging system used to measure field pattern.

The magnitude of the electric field just inside the lens surface, $E_{\mathrm{INT}}(\omega)$, is shown in Fig. 2(a) normalized to unity. Below the critical angle, the P-polarized component of $E_{\mathrm{RFL}}(\omega)$ is 180° out of phase with that of $E_{\mathrm{DIR}}(\omega)$,[30] leading to the field null at $\theta = \theta_c$ along the x- or P-polarized axis. For $\theta > \theta_c$, the $\sin(\theta)$ dependence of the dipole radiation pattern causes the fall-off of the field. For the fully S-polarized radiation, the direct and reflected fields add in phase, leading to a maximum value when the angle of incidence is the critical angle. Beyond critical angle, the S-polarized fields reflected from the interface are out of phase with the direct field. As $|r_s|$ approaches unity for large angles, the total field drops to zero.

The field external to the silicon lens, $E_{\mathrm{ext}}(\omega)$, is determined from $E_{\mathrm{int}}(\omega)$ by the Fresnel transmission coefficients, t_s and t_p,[29] for S- and P-polarized fields with respect to the normal to the lens surface. The external field, normalized to the internal field, is seen in Fig. 2(b), which is displayed on the same relative scale as Fig. 2(a). The field pattern shown was calculated at 0.5 THz but is independent of frequency in the plane-wave approximation used. The increase in magnitude of the field is simply due to transition from a high index ($n = 3.418$)[31] to low index ($n = 1$) medium. As seen from the figure, the field along the x axis, which is fully P polarized, is preferentially coupled out of the lens since it strikes the lens surface near Brewster's angle, $\theta_B = 16.3°$. Internal reflection within the lens represents a major loss mechanism for THz radiation since the field-reflection coefficient, r, at normal incidence is 0.55. At Brewster's angle, $r = 0$ for P polarization but $r = 0.84$ for S polarization, resulting in the field pattern in Fig. 2(b). In a high-index material, Brewster's angle is close to critical angle. For silicon, $\theta_c = 17.1°$. The region beyond critical angle, in which there is assumed to be no coupling from the lens to free space, is represented by the gray surface in Fig. 2(b).

Following previous work by Keiding[17,18] and Mittleman,[20] the far-field pattern is calculated from the scalar field on the lens surface using the Kirchoff–Fresnel diffraction integral.[32] This was evaluated numerically over the lens surface for given single frequencies using a grid size of λ/5 or finer, which was determined to lead to acceptably small numerical errors.

As mentioned by other authors, the lens field-pattern calculation is an approximation since the lens size is not a large number of wavelengths, especially at low frequencies. At low frequencies, a description of field patterns on the lens surface using a plane-wave approximation is no longer accurate. Thus the calculations presented here

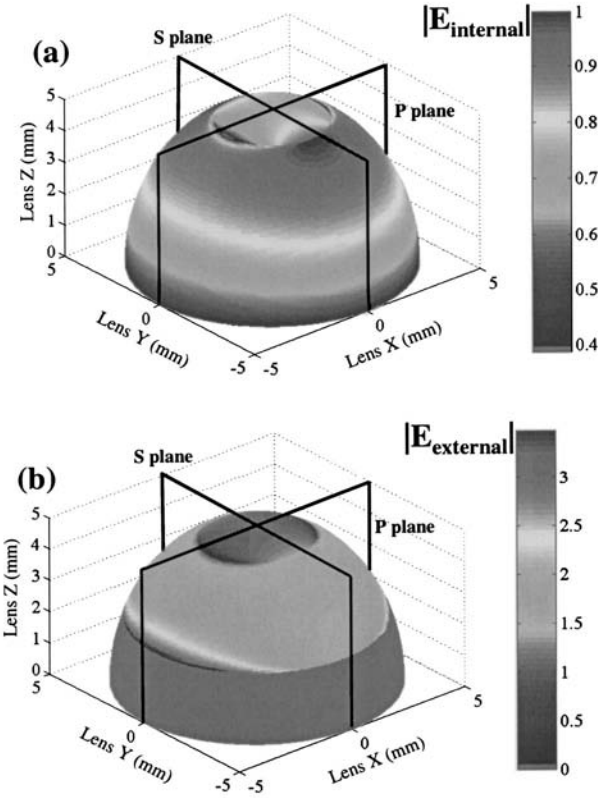

Fig. 2. Calculated electric field amplitude (a) just inside the silicon-lens surface and (b) just exterior to the silicon lens. The *S* plane and *P* planes relative to the dipole orientation are shown in Fig. 1(c).

are qualitative rather than rigorous. Calculated field patterns with distance and frequency corresponding to the measured data are shown as insets to each of the amplitude and phase data sets in Figs. 4, 5, 6, and 8. No floating parameters were used in these calculations.

3. MEASUREMENT OF TEMPORALLY AND SPATIALLY RESOLVED ELECTRIC FIELDS

The experimental setup used to measure the beam profiles of the THz radiation is shown in Fig. 1(b). Optical pulses (~50 fs at 805 nm) are produced by a Ti:sapphire laser and directed by a beam splitter into the THz source (transmitter) and THz detector (receiver). In the transmitter arm, a mechanical shaker[33] operating at 13 Hz provides optical delay. The transmitter consists of a photoconductively switched pair of striplines on semi-insulating GaAs biased at 80 V dc with an optical gating pulse of 7 mW. The generated THz pulse is then collimated by a hemispherical silicon lens before propagating toward the receiver. The specific silicon-lens configuration has been shown to strongly affect the propagation of THz radiation.[20,21] The plano-convex lens used for both the THz source and detector were hemispherical, designed for collimation of THz radiation. The lens heights were 6.56 mm and 6.42 mm for the source and detector respectively, with radii of curvature of 5 mm. Aberrations that arise from the lens geometry strongly affect the THz pulse coupled to free space; these will be discussed in a subsequent paper.

The receiver unit consists of a dipole antenna on oxygen-ion-implanted silicon-on-sapphire[34] coupled to the optical gating pulse through a 2-m, single-mode fiber (3M, 820 nm, 5.5-μm core diameter). To compensate for the group-velocity dispersion in the fiber, the optical beam is precompensated using a grating pair. The optical gating pulse measured after the fiber cable has an autocorrelation width of 120 fs. A 50-μm dipole antenna without a silicon lens to collect incident THz radiation was used for high spatial resolution near the transmitter. The metallic dipole structure is mounted on the side of the chip away from the incident THz beam, facing toward the optical gating pulse, to utilize the n^3 field enhancement of a dipole on a dielectric surface.[25,27] The signal-to-noise ratio for the antenna with no lens at $d = 16\,\mathrm{mm}$ limits the spectral range of measurements to between 0.1 THz and 1.0 THz.

Spatially resolved field measurements to experimentally determine the electric field patterns near the THz source were made in the plane perpendicular to the propagation direction of the THz beam. The field was measured at a distance of $d = 16\,\mathrm{mm}$ from the surface of the silicon lens, as close as the experimental configuration permitted. To spatially resolve the field, the receiver was mounted on an XY stepper stage and raster scanned through the observation plane. A 60×80 grid of $0.24\,\mathrm{mm} \times 0.16\,\mathrm{mm}$ step sizes for a total distance $14.64\,\mathrm{mm} \times 18.66\,\mathrm{mm}$ was measured. The current induced in the receiver antenna by the THz radiation was measured at a sensitivity of 10^9 V/A and filtered to reduce

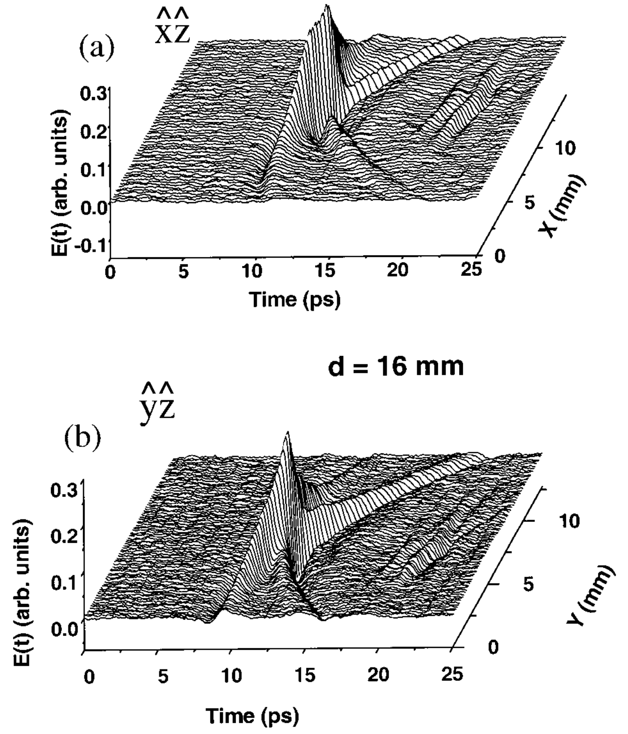

Fig. 3. Measured time-resolved electric field at $d = 16\,\mathrm{mm}$ from source silicon lens. Measured field is shown for (a) the $\hat{x}\hat{z}$ and (b) the $\hat{y}\hat{z}$ planes.

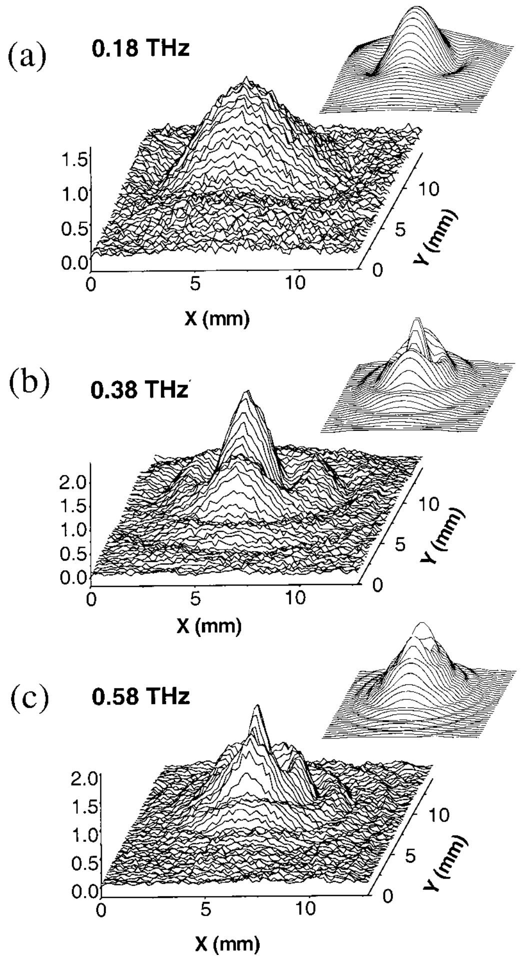

Fig. 4. Spatially resolved electric field amplitudes at frequencies of (a) 0.18 THz, (b) 0.38 THz, and (c) 0.58 THz. Data are measured near the silicon-lens surface at distance $d = 16$ mm. The insets to the figure are the calculated beam profiles.

noise before averaging 64 times to increase the signal-to-noise ratio. The time-resolved electric field measured is shown in Fig. 3 for horizontal ($\hat{x}\hat{z}$ or P plane) and vertical ($\hat{y}\hat{z}$ or S plane) cross sections through the center of the beam (origin). The pulse measurement has a cylindrical symmetry rotated around the central axis of propagation.

A numerical Fourier transformation applied to the time-resolved data at each spatial point generates the complex amplitude for each frequency within the system bandwidth. This permits the field amplitude and relative phase at specific frequencies to be experimentally determined in the plane of measurement, ideally normal to beam propagation. We are able to make these measurements because our experimental system provides phase-coherent detection.

The amplitude, Fig. 4, and phase distributions, Fig. 5, of the field 16 mm from the lens are shown for three frequencies: 0.18, 0.38, and 0.58 THz. The tilt in the phase measurements in Fig. 5 is due to a 2° to 3° experimental misalignment of the plane of propagation with respect to the plane of detection or a 0.2-mm shift in the z direction over the total range of a 5.2-mm scan. The precise tilt of the phase front is difficult to obtain due to the prominent features in the phase measurements. Both the spatially resolved amplitude and phase exhibit more structure than expected for a simple Gaussian profile pulse[17]; such amplitude structure has been observed by previous authors. The complexity of the structure in the amplitude profile increases with higher frequencies and becomes more sharply peaked spatially; lower frequencies maintain a generally Gaussian shape. Similar frequency dependence is seen in the spatially resolved phase where higher frequencies exhibit a more tightly spaced ring structure, which matches that of the amplitude profile. The phase structures observed here can arise from a summation of high-order, non-TEM modes, and the physical origin will be addressed in a future paper. The theoretically predicted amplitude and phase distributions (insets of Figs. 4 and 5) qualitatively match the measured field distributions for the frequencies shown.

Since the experimentally limited 16-mm measurement distance corresponds to several tens of wavelengths, an independent method of observing the field pattern directly at the silicon lens is desired. A method to observe the theoretically predicted field pattern at the silicon lens is to observe the field distributions at an image plane of the beam. This can be done as shown in Fig. 1(c) using a pair of 119-mm focal-length paraboloidal mirrors as a

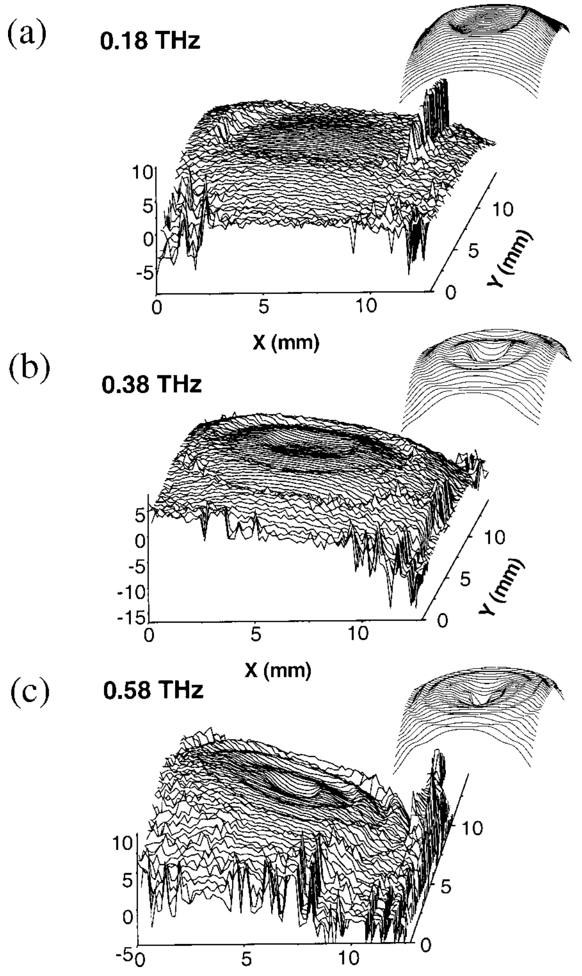

Fig. 5. Spatially resolved electric field phase corresponding to the amplitude profiles of Fig. 7: (a) 0.18 THz, (b) 0.38 THz, and (c) 0.58 THz. The insets to the figure are the calculated phase distributions.

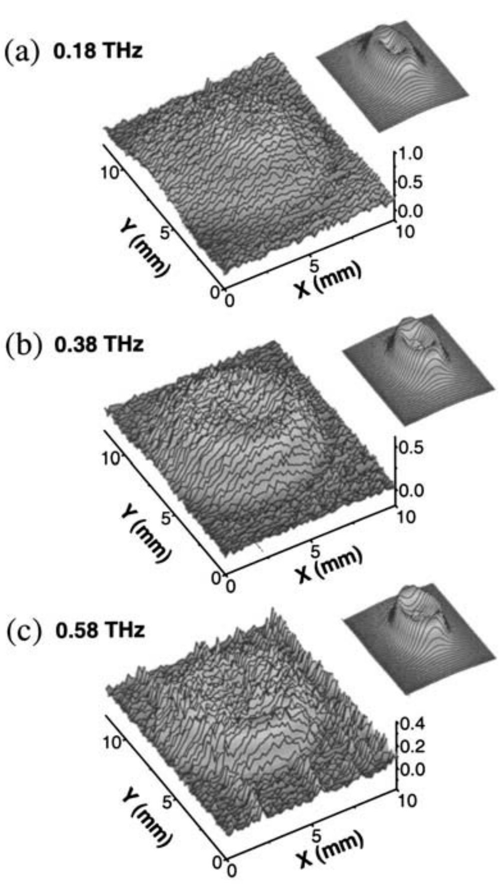

Fig. 6. Measured THz beam amplitude profiles at frequency-independent waist size image plane, Fig. 1(c). The insets show the theoretically calculated lens patterns after propagating a distance of 1 mm.

unity conjugate ratio imaging system. While the initial beam waist, w_{01}, is frequency independent, the second beam waist, w_{02}, has a frequency-dependent amplitude distribution. The third waist, w_{03}, is a 1:1 image of w_{01} assuming matched foci for the optical system and proper system alignment. Although a perfect image is formed by ideal mirrors, the finite 50-mm diameters of the mirrors add an aperture to the optical system. This aperture will incur the loss of phase information and peripheral amplitude, so the complex field at the transmitter lens will not be perfectly imaged. The third waist, w_{03}, is where the receiver is located in a typical nonspatially resolved TDS measurement system for highest signal strength.

Figure 6 shows the results of the measured beam profile for frequencies of 0.18, 0.38, and 0.58 THz, respectively, at the frequency-independent focus, w_{03}. As expected for an initially frequency-independent beam waist, the radius of the measured amplitude distribution demonstrates a near-frequency-independent radius. If the system is aligned properly to maximize the optical transfer function, the second focus should be an image of the intensity distribution at the surface of the transmitter silicon lens. A toroidal structure is seen in the intensity in good agreement with the theoretical results of Fig. 2(b). The low signal-to-noise ratio of the receiver without a collection lens in this configuration precluded determination of the phase.

The insets of Fig. 6 show the calculated field distribution at a plane 1 mm from the tip of the lens (w_{01}) calculated from the model presented earlier. Qualitative agreement between the measured and predicted beam profiles are quite good. It can be seen by comparing the planar field profiles 1 mm from the lens (Fig. 6 insets) to the frequency-independent field on the lens surface (Fig. 2) that diffraction broadens the beam profile after short propagation distances. Diffraction plays a larger role at the lower frequencies. The lowest-frequency measured and calculated field profiles do not match well because the imaging system has introduced apertures, losing phase and amplitude information. Additionally, the model, which used a plane-wave approximation to calculate field profiles, will not be as accurate for longer wavelengths.

4. PROPAGATION OF TERAHERTZ BEAMS

To determine the effects of propagation on the THz beam, the spatially resolved field was measured at two propagation distances, $d = 116\,\mathrm{mm}$ and $d = 216\,\mathrm{mm}$, using the experimental configuration shown in Fig. 1(b). The THz receiver was a 50-μm dipole antenna identical to the dipole antenna of the exposed receiver; however, a reduced-aperture silicon lens was added to increase the measured signal strength. A 1.5-mm-diameter aperture was fashioned through metal evaporation of a 200-nm-thick coating of aluminum directly on the silicon lens. The effect of this aperture is twofold. First, it increases the spatial resolution of the measurement. Second, since the dipole receiver antenna is placed at the focal point of the lens, the antenna sees the Fourier transform of the field pattern over the lens aperture. By reducing the aperture, or spatial area over which the field is integrated, the Fourier-plane pattern is broadened, reducing the sensitivity to the angle of incidence of the incoming radiation. Hence the reduced-aperture lens has a less sharply peaked directivity than an unmodified lens has. Using the reduced-aperture lens, measurements were made in a 33×33 grid with step sizes $1.46\,\mathrm{mm} \times 1.44\,\mathrm{mm}$, respectively, for a total area of $48.18\,\mathrm{mm} \times 47.52\,\mathrm{mm}$. Representative time-resolved field measurements in horizontal ($\hat{x}\hat{z}$) and vertical ($\hat{y}\hat{z}$) planes taken at a propagation distance $d = 116\,\mathrm{mm}$ are shown in Fig. 7.

The spatial resolution of the reduced-aperture system is limited by the size of the aperture, 1.5-mm diameter. Measurements have demonstrated that the dipole receiver without a lens and the receiver with a reduced-aperture lens yield comparable beam profiles, providing that the spatial variation of the field amplitude is small compared with the aperture diameter. The reduced-aperture lens and receiver system increases the signal-to-noise ratio by a factor of 5 over a receiver with no lens, and is necessary, considering the decrease in field strength after free-space propagation. However, compared with a silicon lens with no aperture, the reduced-aperture system attenuates signal strength below 0.3 THz, limiting the bandwidth range from 0.4 to 1.5 THz. Thus the 1.5-mm aperture provides a compromise between a less directive receiver with increased spatial resolution and signal strength.

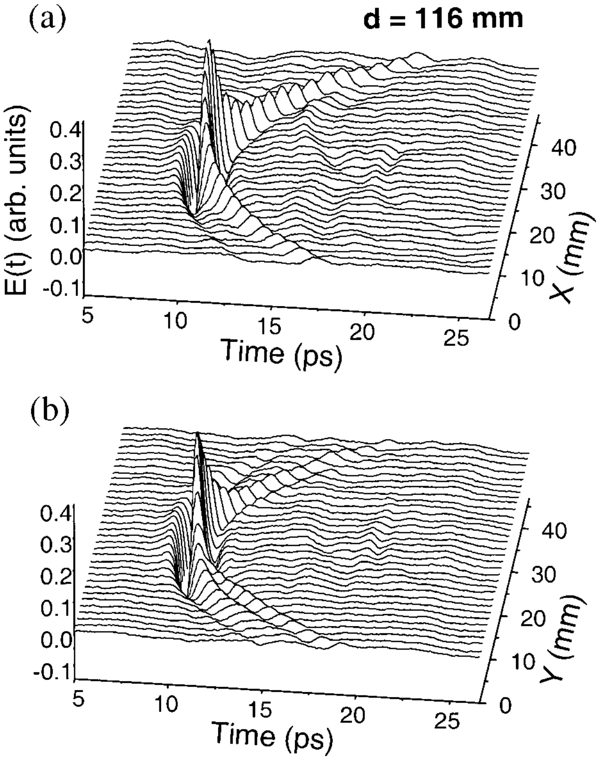

Fig. 7. Measured time-resolved fields using a reduced-aperture silicon lens in the (a) xz and (b) yz planes shown in Fig. 1 at a distance $d = 116$ mm from the silicon lens.

By decreasing the angular sensitivity of the THz receiver, the directivity of the receiver antenna can be neglected in these measurements. The directivity of the receiver was measured as a function of angle to the maximum angle between THz source and receiver of 12° at $d = 116$ mm. Over this range, the directivity contributes less than 3% variation in field-amplitude profile across the beam in the frequency range. However, directivity would be a significant concern if the receiver were equipped with a full-aperture lens,[21] where the variation across the same range would be 5 to 20 times greater with a strong frequency dependence.

The time-resolved measurements were converted to complex frequency profiles by a numerical Fourier transform. Figure 8 shows the magnitude of the electric-field amplitude measured at three frequencies. The beams appear roughly Gaussian, with the lower frequencies diffracting more strongly than the higher frequencies at a given distance, as expected. Also observable is ringlike structure around the base of the amplitude distribution, similar in appearance to diffraction rings, which tend to grow less prominent with increasing distance, d. These have been previously observed in one-dimensional measurements.[17,18,20,21] The spatially resolved phase was measured for the amplitude distributions shown and was found to have a nearly spherical profile with a radius of curvature close to that expected for a Gaussian beam, within a 10% variation of that expected from a purely lowest-order profile.

To understand propagation of the THz beam, we initially attempt to model the beam as a TEM$_{00}$ Gaussian. At optical frequencies, the spatially resolved intensity distribution of Gaussian beams is measured. The field magnitude is then given by the square root of the intensity. Although phase is not directly determined, it can be calculated assuming that there is a planar phase front at the beam waist. Following this procedure, we directly measure the field amplitude at $d = 116$ mm and 216 mm for each discrete frequency over the range 0.4 to 1.5 THz. The measured spatially resolved field magnitude is then fit numerically to a TEM$_{00}$ Gaussian beam profile. Three fit parameters are used: the beam waist, w_0, distance from the waist, z, and amplitude, E_0, at a given frequency, since these completely determine a TEM$_{0,0}$ Gaussian beam. The beam waist is assumed to have a frequency-independent diameter[35] and a planar phase front located at the apex of the silicon lens on the THz source. This assumption is made because, in the plane-wave treatment of lens field patterns (Section 2), all frequencies have a constant waist size and near planar phase front at the silicon lens.

The validity of using this simple model, a TEM$_{00}$ Gaussian with a frequency-independent waist, to describe the THz beam is tested by comparing the measured frequency-dependent beam size to the propagation relations for Gaussian beams.[23] From the measured $|E(\omega, z)|_{z=d}$, we extract the beam radius, $w(\omega, z)|_{z=d}$, by applying a least-squares iterative fitting method to find the TEM$_{00}$ Gaussian distribution that most closely matches the measured profile. Numerically determined beam radii as a function of frequency for the series of measurements are shown as points in Fig. 9.

Figure 9(a) shows the measurements taken at $d = 116$ mm. The increased beam radius for the lower fre-

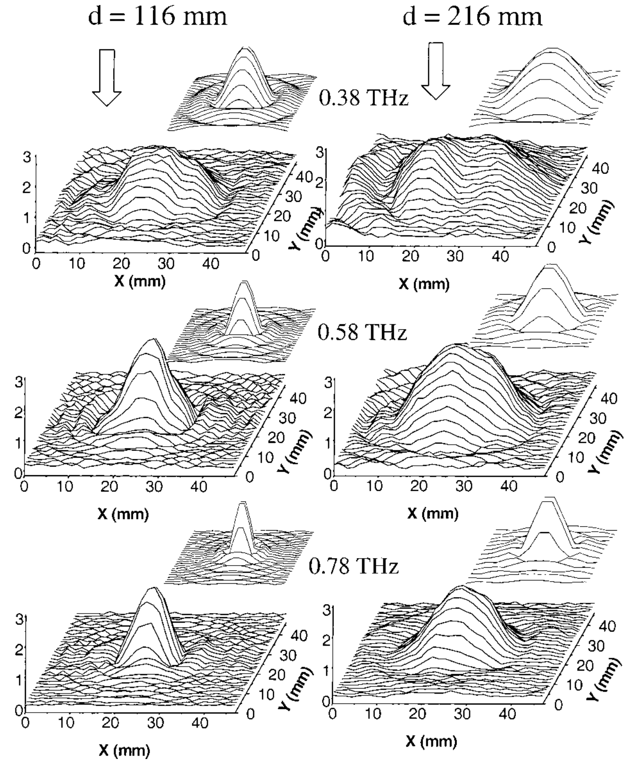

Fig. 8. Spatially resolved electric field amplitudes at frequencies of (a) 0.38 THz, (b) 0.58 THz, and (c) 0.78 THz. Data are measured at distances $d = 116$ mm (left) and $d = 216$ mm (right). The insets to the figure are the calculated beam profiles.

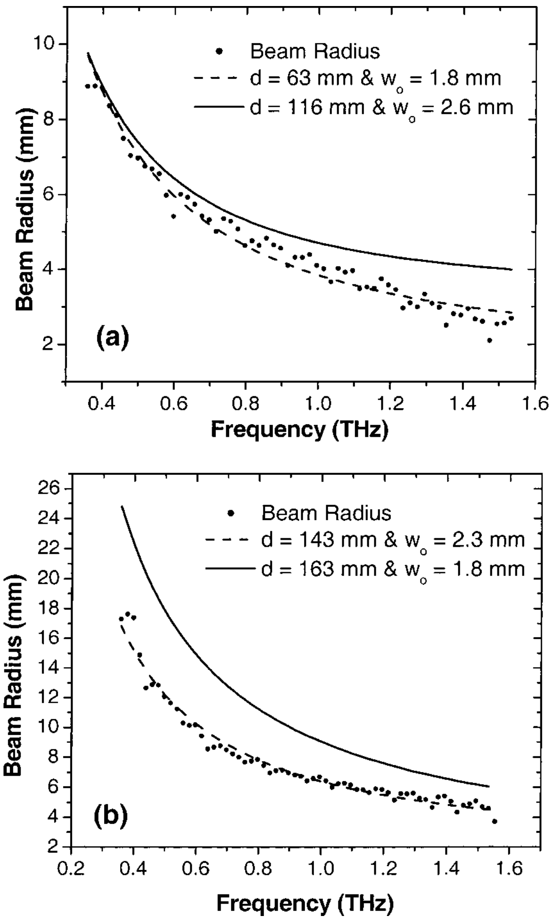

Fig. 9. Measured waist radius (points) as a function of frequency at (a) 116 mm and (b) 216 mm. The solid curve is the best fit to TEM_{00} Gaussian beam obtained with fit parameters (a) $d_{\mathrm{fit}} = 63\,\mathrm{mm}$ and (b) $d_{\mathrm{fit}} = 147\,\mathrm{mm}$. The dashed curve is the best fit obtained for the experimentally measured distances, d.

quencies is due to diffraction, as would be expected for a broad-bandwidth beam with a frequency-independent waist. If the distance for the numerical fit is fixed at $d = 116\,\mathrm{mm}$, the best least-squares-fit beam waist is $w_0 = 2.6\,\mathrm{mm}$ (solid curve), in disagreement with the measurements at high frequencies. The measured beam is narrower than expected at this range assuming a TEM_{00} profile. The best least-squares fit, floating both the propagation distance and beam-waist parameters, required that $w_0 = 1.8\,\mathrm{mm}$ (dashed curve) and a corresponding distance of $d_{\mathrm{fit}} = 63\,\mathrm{mm}$ from the waist. The propagation distance assigned by the best fit differs by nearly a factor of 2 from the actual measurement distance, d.

For measurements at $d = 216\,\mathrm{mm}$, the solid curve in Fig. 9(b) shows the predicted beam radius if the values of $w_0 = 1.8\,\mathrm{mm}$ and $d_{\mathrm{fit}} = 63\,\mathrm{mm}$ determined above are taken as the initial conditions for a Gaussian beam and the beam is propagated an additional 100 mm. Comparison of the measured amplitude distribution to the beam profile calculated shows the beam is again less divergent than predicted. The best fit for data measured at 216 mm returns a beam waist of $w_0 = 2.3\,\mathrm{mm}$ at a distance of $d_{\mathrm{fit}} = 142\,\mathrm{mm}$. The distance returning the best fits for data measured at 116 mm and 216 mm differ by 74 mm; the beam appears to have propagated 26 mm less than the actual distance of 100 mm.

Propagation of a broad-bandwidth THz beam under our experimental conditions cannot be accurately described by a TEM_{00} Gaussian beam with a frequency-independent waist determined from the intensity or magnitude of the electric field. Simple Gaussian propagation predicts a beam diameter 140% larger than measured. Although not shown here, use of a frequency-dependent beam waist also fails to predict propagation for TEM_{00} Gaussian beam fits at fixed distances.

The calculated field pattern exterior to the silicon lens, shown in Fig. 7, indicates that the electric field giving rise to the THz beam has rapid spatial amplitude variations. Beams with arbitrary spatial variations can be described mathematically as a superposition of Hermite–Gauss modes for Cartesian symmetry or Laguerre–Gauss modes for cylindrical symmetries. In this description, the beam radius, $w(z)$, and radius of curvature, $R(z)$, are the same for all modes. By describing the beam as such a superposition, each orthogonal mode can be propagated through any optical system describable by a matrix.[23] Since both the Hermite–Gauss and the Laguerre–Gauss basis sets form a complete set of solutions to the propagation equation, the matrix method can thus be used to propagate arbitrarily complex beams in the paraxial approximation.[35] Due to the cylindrical symmetry of the measured beam profiles, we use the Laguerre–Gauss modes to represent the THz beam. Similar results can be obtained from the Hermite–Gauss basis set; however, many more modes are needed to accurately represent the beam.

The measured spatially resolved complex electric field for fixed distance, z, at a given frequency, ω, is $E_{\mathrm{meas}}(x, y, \omega)$. The field distribution of a given Laguerre–Gauss mode at a given distance, z, is a function of the frequency, ω, radial mode, n, angular mode, ℓ, and position given in cylindrical coordinates by r, ϕ. The distribution, $E_{n\ell}(r, \phi, w_0, \omega)$, is given by[23]

$$E_{nl}(r, \phi, \omega) = \sqrt{\frac{2n!}{\pi(n + |l|)}}\,\frac{\exp\{j(2n + l + 1)[\psi(z) - \psi_0]\}}{w(z)} \times \left[\frac{\sqrt{2}r}{w(z)}\right]^{l} L_n^{l}\left[\frac{2r^2}{w(z)^2}\right] \exp\left[-jk\frac{r^2}{2q(z)} + il\phi\right]. \quad (1)$$

Here k is the wave vector in free space, ω/c. The complex beam parameter is $q(z) = 1/R(z) - j\lambda/\pi w(z)^2$, with $R(z)$ the radius of curvature of the beam at axial point z and $w(z)$ the beam radius. $\psi(z)$ is the phase angle of $q(z)$, $\tan(\psi) = \pi w(z)^2/\lambda R(z)$, and ψ_0 is the phase at the beam waist. We use Cartesian coordinates in the representation of the data to reflect the rectangular grid of measured points, while the modal fields are represented in the cylindrical coordinate system of the Laguerre–Gauss modes. The THz beam is decomposed into normalized Laguerre–Gauss modes, $E_{n\ell}(r, \phi, w_0, \omega)$, multiplied by a complex amplitude, $A_{n\ell}$, determined from the overlap integral of the measured spatially resolved field with a given modal component:

$$A_{n\ell} = \iint E^{*}_{n\ell}(r,\ \phi,\ w_{\mathrm{o}},\ \omega) E_{\mathrm{meas}}(x,\ y,\ \omega) \partial r \partial \phi. \tag{2}$$

Overlap integrals are performed with trapezoidal rule integration in Matlab. Each mode is normalized such that the overlap integral of a mode, $E_{n\ell}(r,\ \phi,\ w_{\mathrm{o}},\ \omega)$, with itself gives a complex amplitude $A_{n\ell} = 1$, symbolizing a complete overlap of the two distributions. The overlap integral of two dissimilar modes, $E_{n\ell}(r,\ \phi,\ w_{\mathrm{o}},\ \omega)$ and $E_{mp}(r,\ \phi,\ w_{\mathrm{o}},\ \omega)$ with $m \neq n$ and $p \neq \ell$, yields $A_{n\ell} = 0$. The magnitude of the complex amplitude, $A_{n\ell}$, determines the relative fraction of the Laguerre–Gauss modal component, while the phase determines the spatial orientation of the Laguerre–Gauss mode pattern in the coordinate system.

To determine propagation of THz pulses, we calculate the electric-field distribution from an experimentally de-

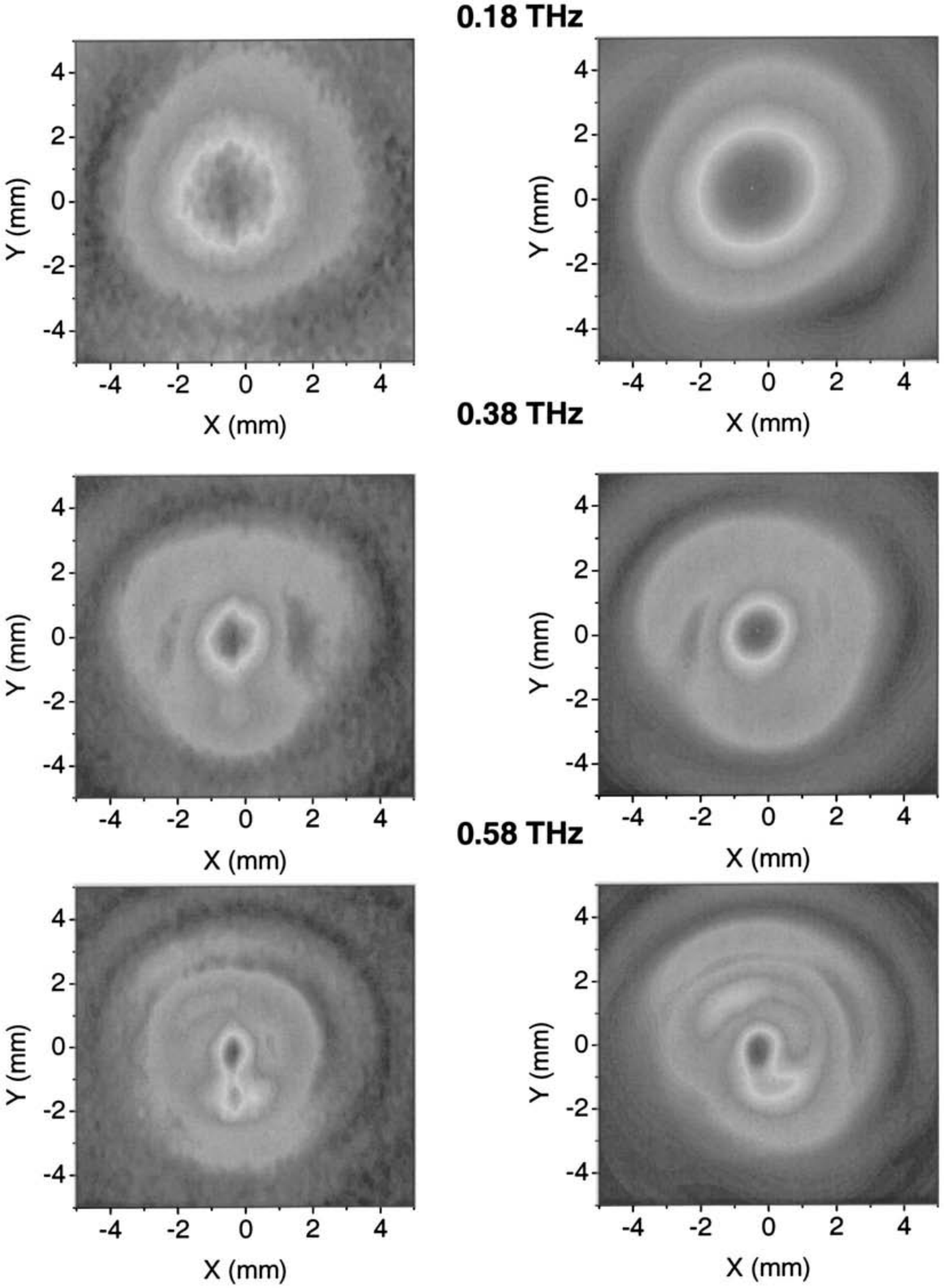

Fig. 10. Comparison of measured electric field amplitude distributions (left column) with amplitude distribution determined from a decomposition into Laguerre–Gauss modes (right column.) Data are the same as Fig. 4, $d = 16$ mm for frequencies of (a) 0.18 THz, (b) 0.38 THz, and (c) 0.58 THz.

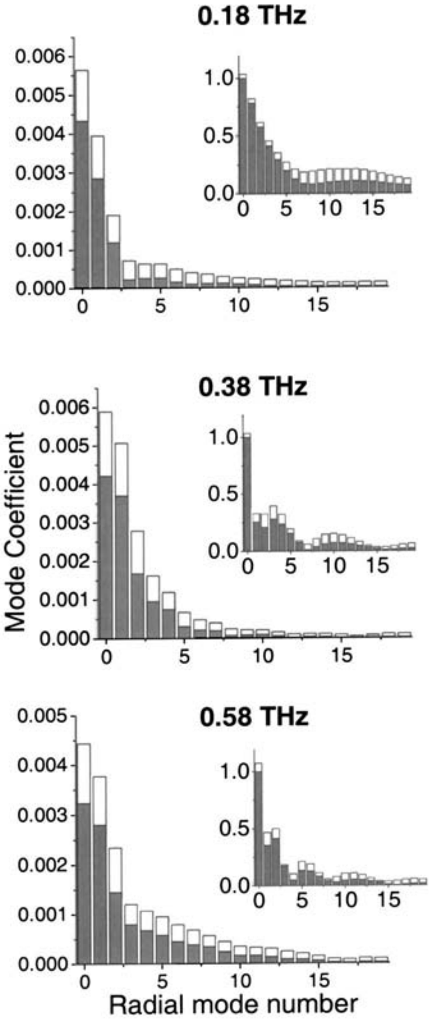

Fig. 11. Amplitude of Laguerre–Gauss modes from Fig. 10. The dark bar represents the zeroth angular mode, while the light-colored bar is total amplitudes of angular modes from 1 to 4. The insets are the modal decomposition of the corresponding theoretically calculated field distributions (insets of Figs. 4 and 5).

termined summation of Laguerre–Gauss modes. Calculating the modal decomposition from measured amplitude profiles, two parameters are not completely determined. These are the position of the coordinate axis origin of the data set, and the waist radius, w_o. Accurate determination of the modal amplitudes is strongly dependent upon the x, y origin of the data coordinate system being coincident with the r, ϕ origin of the n, ℓ mode. The waist value is not as critical; in theory any waist size can be used. However, a judicious choice of a "correct" waist minimizes the number of required modes and can change the propagation characteristics depending upon the number of modes used in propagation calculations. The calculated field is determined from the summation of all modes that could be determined from the experimental data:

$$E_{\text{calc}}(x, y, \omega) = \sum_{n=0}^{N} \sum_{\ell=0}^{L} A_{n\ell}(\omega) E_{n\ell}(r, \phi, w_o, \omega) \times \exp(-jkz). \tag{3}$$

Although overlap integrals were calculated up to modes $N = 200$ and $L = 50$, amplitudes are shown only for $N = 20$ and $L = 5$ since $A_{n\ell}$ values reach the noise limit of the data for large values of n and ℓ. To determine the coordinate axis origin of the data set, the least-squares fit of E_{meas} and E_{calc} was optimized by letting the origin of the

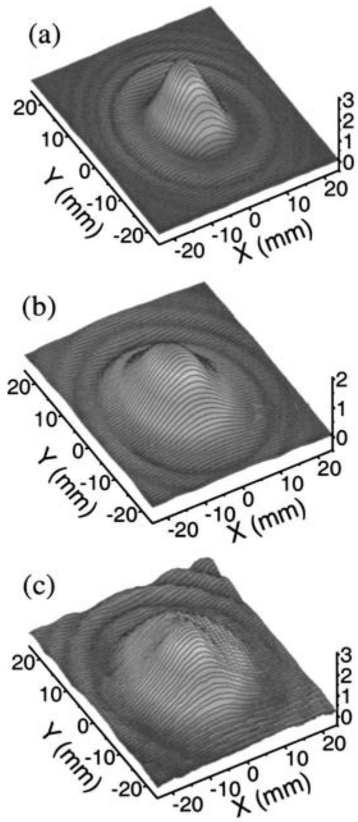

Fig. 12. (a) THz beam amplitude profiles at 0.58 THz generated from experimentally determined Laguerre–Gauss modes, A_{nl}, at $d = 116$ mm of Fig. 10. (b) These modes are used to predict the amplitude profile at $d = 216$ mm. (c) The measured amplitude profile at $d = 216$ mm.

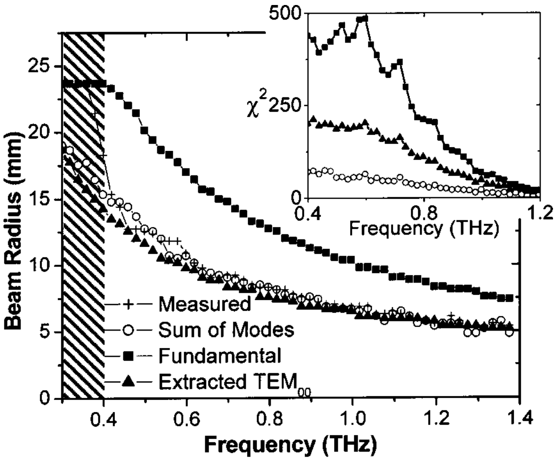

Fig. 13. Beam radius from propagated multimode and single mode compared with measured data at $d = 216$ mm. The extracted TEM_{00} mode was determined by Laguerre–Gauss decomposition. The inset shows the fitting figure of merit as determined by the least-squares method.

data set float. The beam-center position determined this way was more accurate than beam centers determined through center-of-mass calculations directly on data sets. The position of the beam center that gave the best fit to the data additionally minimized the number of modes with amplitude $A_{n\ell}$ above the noise base. A similar procedure was used to determine the optimal, but not unique, beam waist, w_o, used for modal-amplitude determination. This choice of waist is somewhat arbitrary, choosing a different beam waist would give different modal distributions but generate equally valid results.

Figure 10 compares the amplitude profiles, $|E(x, y)|$, measured at $d = 16$ mm (left column) to the profiles determined from a superposition of Laguerre–Gauss modes using modal amplitudes, $A_{n\ell}$, determined from Eq. (2). To accurately determine the $A_{n\ell}$ coefficients and minimize the number of modes, the experimental artifact of phase-front tilt (Fig. 5) has been numerically removed from the data. The generated mode amplitudes, $|A_{n\ell}|$, for the measured and calculated field distributions are shown for comparison in Fig. 11 for frequencies of 0.18, 0.38, and 0.58 THz. The lowest angular order ($\ell = 0$) is shown as a dark bar, and contributions from higher angular modes ($\ell = 1, 2, 3, 4$) are grouped together in the white bar for clarity. The lowest angular orders clearly dominate the modal distribution. For all frequencies, the modal structure is similar—a distribution of low-order modes, followed by a null, and a second distribution of higher-order modes. The grouping of low-order modes corresponds to the central peak seen in all figures. The higher-order modes may correspond to the annular ring structure(s).[36] These features are not well resolved in the measured data.

By describing the THz beam as a superposition of Laguerre–Gauss modes, it is possible to accurately determine propagation of THz beams. The measured THz beam profiles at given frequencies were described as a superposition of Laguerre–Gauss modes, each with a waist radius of 2 mm. Since modes share a common waist size, the mode-dependent spatial field distribution results in each mode diffracting differently, and spatial reshaping of the beam occurs with propagation. Superposition of several Laguerre–Gauss modes leads to destructive interference between higher-order modes in the wings of the beam, resulting in a steeper spatial profile than that described by a TEM_{00} Gaussian alone.

To demonstrate that the modal decomposition reproduces the THz beam profile following THz beam propagation, the amplitude profile calculated from the experimentally determined Laguerre–Gauss modal amplitudes at $d = 116$ mm, and $f = 0.58$ THz is shown in Fig. 12(a). The same modal amplitudes, $A_{n\ell}$, are then used to determine the predicted beam profile at a distance, $d = 216$ mm, using 20 radial and 5 angular modes. The field pattern predicted from propagation of the mode superposition agrees well with the measured amplitude profile at $d = 216$ mm, and $f = 0.58$ THz, shown in Fig. 12(c). Similar results are obtained for other frequencies and modes.

Figure 13 compares the amplitude 1/*e* widths of the measured and predicted beam profiles for propagation and measurements made at $d = 216$ mm. The measured beam radius is shown as plus symbols (+). The propagated superposition of modes, where each Laguerre–Gauss mode (20 angular and 5 radial) is determined at $d = 116$ mm and propagated to 216 mm before summation, is shown as open circles. The sum of modes shows a good match over the valid range of 0.4 to 1.4 THz, assuming a beam waist radius of 2 mm. The measured beam radius (+) diverges from predictions at low frequencies due to limited signal-to-noise ratio and aperture sizes of the order of a wavelength.

To demonstrate the effect of modes on beam propagation, we plot the beam radius of only the fundamental Laguerre–Gauss mode ($n = 0, \ell = 0$), corresponding to a TEM_{00} Gaussian, as solid squares in Fig. 13. Using only the fundamental mode, the predicted beam radius is much larger than measured, mirroring the results of Fig. 9(b). This illustrates spatial profile steepening caused by the interference between modes discussed above.

Extracting the $n = 0, \ell = 0$ mode from the measured complex-field profile can provide a relatively simple method for estimating the beam radius (1/*e* point). The solid triangles in Fig. 13 shows the predicted beam radius as a function of frequency propagated from 116 mm to 216 mm using a larger beam waist of $w_o = 3.65$ mm in Eq. (2) to determine the A_{00} modal amplitude. By increasing the beam waist used for determining individual modal amplitudes, the resultant beam has less diffraction and remains more spatially confined. This is fundamentally different to the fitting procedure used in Fig. 9. Figure 9 shows the results of fitting a single Gaussian mode to an electric field profile formed of a superposition of higher-order modes, as shown in Eq. (3). In other words, a TEM_{00} mode was fit to the superposition of all modes. Here the Laguerre–Gauss derived TEM_{00} mode is extracted from the measured profile, and the higher-order modes are ignored. Our ability to extract the TEM_{00} mode from the THz beam profile through a Laguerre–Gauss decomposition is due to the ability to experimentally measure phase to a precision limited by the signal-to-noise ratio and dynamic range of the data.

The accuracy of these approximations is shown in the inset of Fig. 13. The relative match between measured and propagated complex beam amplitude profiles is compared by performing a least-squares fit over the entire beam profile. The accuracy of the fit is determined by the magnitude of χ^2, which is zero for a perfect reconstruction of the entire beam profile. The extracted TEM_{00} mode (inset solid triangles), which predicts only the beam radius, performs poorly in comparison to the sum of Laguerre–Gauss modes (inset open circles). Fitting a fundamental mode to the measured field magnitude distribution (inset solid squares) does not predict the beam radius or the beam profile. Thus higher-order modes must still be considered in the cases where an accurate representation of the beam profile undergoing propagation is required, such as at a focus of an optical system.

5. CONCLUSION

Measurements of the complex spatial amplitude distribution of optoelectronically generated THz beams indicate that the beam does not behave like a TEM_{00} Gaussian.

THz beams can exhibit complex spatial profiles, particularly in the near field or in image planes, which must be considered in applications of lens-coupled THz sources where field patterns are important, such as ranging or coupling into waveguides. The complex-field pattern also affects the propagation of THz beams that are less divergent than predicted by a simple $\mathrm{TEM}_{0,0}$ approximation. The THz beam profile can be represented as a sum of approximately 50 Laguerre–Gauss modes that accurately predicts propagation of the complex beam profile. However, for rough calculations extracting the lowest order, the $\mathrm{TEM}_{0,0}$ mode accurately predicts the spatial dimension, but not the shape, of a freely propagation THz beam.

This work was supported by the National Science Foundation (ECS-9984896) by the U.S. Army Research Office (DAAD19-99-R-BAA8), and by the U.S. Department of Energy. The authors would like to acknowledge Wendy Siemens, currently with Sandia National Labs, and Kati McClatchey, who contributed technical support as undergraduate students. Kati McClatchey acknowledges support from the National Science Foundation Research Experience for Undergraduates program for support during this project.

REFERENCES

1. M. van Exter, C. Fattinger, and G. Grischkowsky, “High-brightness terahertz beams characterized with an ultrafast detector,” Appl. Phys. Lett. **55**, 337–339 (1989).
2. D. H. Auston, K. P. Cheung, and P. R. Smith, “Picosecond photoconducting Hertzian dipoles,” Appl. Phys. Lett. **45**, 284–286 (1984).
3. H. Harde, R. A. Cheville, and D. Grischkowsky, “Terahertz studies of collision-broadened rotational lines,” J. Phys. Chem. A **101**, 3646–3660 (1997).
4. T. I. Jeon and D. Grischkowsky, “Nature of conduction in doped silicon,” Phys. Rev. Lett. **78**, 1106–1109 (1997).
5. R. A. Cheville, R. W. McGowan, and D. Grischkowsky, “Time resolved measurements which isolate the mechanisms responsible for terahertz glory scattering from dielectric spheres,” Phys. Rev. Lett. **80**, 269–272 (1998).
6. D. M. Mittleman, R. H. Jacobsen, and M. C. Nuss, “T-ray imaging,” IEEE J. Sel. Top. Quantum Electron. **2**, 679–692 (1996).
7. R. Mendis and D. Grischkowsky, “Undistorted guided-wave propagation of subpicosecond terahertz pulses,” Opt. Lett. **26**, 846–848 (2001).
8. R. W. Ziolkowski, I. M. Besieris, and A. M. Shaarawi, “Aperture realizations of exact solutions to homogeneous wave solutions,” J. Opt. Soc. Am. A **10**, 75–87 (1993).
9. A. E. Kaplan, “Diffraction-induced transformation of near-cycle and subcyle pulses,” J. Opt. Soc. Am. B **15**, 951–956 (1998).
10. D. You and P. H. Bucksbaum, “Propagation of half-cycle FIR pulses,” J. Opt. Soc. Am. B **14**, 1651–1655 (1997).
11. S. Hunsche, S. Feng, H. G. Winful, A. Leitenstorfer, M. C. Nuss, and E. P. Ippen, “Spatiotemporal focusing of single-cycle light pulses,” J. Opt. Soc. Am. A **16**, 2025–2028 (1999).
12. P. Kuzel, M. A. Khazan, and J. Kroupa, “Spatiotemporal transformations of ultrashort terahertz pulses,” J. Opt. Soc. Am. B **16**, 1795–1800 (1999).
13. J. Bromage, S. Radic, G. P. Agrawal, C. R. Stroud, P. M. Fauchet, and R. Sobolewski, “Spatiotemporal shaping of terahertz pulses,” Opt. Lett. **22**, 627–629 (1997).
14. R. W. McGowan, R. A. Cheville, and D. Grischkowsky, “Direct observation of the Gouy phase shift in THz impulse ranging,” Appl. Phys. Lett. **76**, 670–672 (2000).
15. S. Feng, H. G. Winful, and R. W. Hellwarth, “Gouy shift and temporal reshaping of focused single-cycle electromagnetic pulses,” Opt. Lett. **23**, 385–387 (1998).
16. E. Budiarto, N.-W. Pu, S. Jeong, and J. Bokor, “Near-field propagation of terahertz pulses from a large-aperture antenna,” Opt. Lett. **23**, 213–215 (1998).
17. P. U. Jepsen and S. R. Keiding, “Radiation patterns from lens-coupled terahertz antennas,” Opt. Lett. **20**, 807–809 (1995).
18. P. U. Jepsen, R. H. Jacobsen, and S. R. Keiding, “Generation and detection of terahertz pulses from biased semiconductor antennas,” J. Opt. Soc. Am. B **13**, 2424–2436 (1996).
19. A. Gurtler, C. Winnewisser, H. Helm, and P. U. Jepsen, “Terahertz pulse propagation in the near field and the far field,” J. Opt. Soc. Am. A **17**, 74–83 (2000).
20. J. Van Rudd, J. L. Johnson, and D. M. Mittleman, “Cross-polarized angular emission patterns from lens-coupled terahertz antennas,” J. Opt. Soc. Am. B **18**, 1524–1533 (2001).
21. J. Van Rudd and D. M. Mittleman, “Influence of substrate-lens design in terahertz time-domain spectroscopy,” J. Opt. Soc. Am. B **19**, 319–329 (2002).
22. J. T. Verdeyen, *Laser Electronics* (Prentice-Hall, Englewood Cliffs, N.J., 1995).
23. A. E. Siegman, *Lasers* (University Science, Mill Valley, Calif., 1986).
24. D. R. Grischkowsky, “Optoelectronic characterization of transmission lines and waveguides by terahertz time-domain spectroscopy,” IEEE J. Sel. Top. Quantum Electron. **6**, 1122–1135 (2000).
25. W. Lukosz and Z. S. Eth, “Light emission by magnetic and electric dipoles close to a plane dielectric interface. III. Radiation patterns of dipoles with arbitrary orientation,” J. Opt. Soc. Am. **69**, 1495–1503 (1979).
26. R. W. P. King and G. S. Smith, *Antennas in Matter* (MIT Press, Cambridge, 1981).
27. D. B. Rutledge and M. S. Muha, “Imaging antenna arrays,” IEEE Trans. Antennas Propag. **30**, 535–540 (1982).
28. S. Ramo, J. R. Whinnery, and T. Van Duzer, *Fields and Waves in Communications Electronics* (Wiley, New York, 1984).
29. M. Born and E. Wolf, *Principles of Optics*, 7th ed. (Cambridge University, New York, 1999).
30. E. Hecht, *Optics* (Addison-Wesley, San Francisco, Calif., 2002).
31. D. Grischkowsky, S. Keiding, M. van Exter, and C. Fattinger, “Far-infrared time-domain spectroscopy with terahertz beams of dielectrics and semiconductors,” J. Opt. Soc. Am. B **7**, 2006–2015 (1990).
32. J. W. Goodman, *Introduction to Fourier Optics*, 2nd ed. (McGraw-Hill, New York, 1996).
33. D. C. Edelstein, R. B. Romney, and M. Scheuermann, “Rapid programmable 300 ps optical delay scanner and signal-averaging system for ultrafast measurements,” Rev. Sci. Instrum. **62**, 579–583 (1991).
34. M. T. Reiten, K. McClatchey, D. Grischkowsky, and R. A. Cheville, “Incidence-angle selection and spatial reshaping of terahertz pulses in optical tunneling,” Opt. Lett. **26**, 1900–1902 (2001).
35. H. Kogelnik and T. Li, “Laser beams and resonators,” Appl. Opt. **5**, 1550–1567 (1966).
36. C. J. R. Sheppard and T. Wilson, “Gaussian-beam theory of lenses with annular aperture,” IEE J. Microwaves, Opt. Acoust. **2**, 105–112 (1978).